Dynamical stability of quasitoroidal differentially rotating neutron stars

Pedro L. Espino,[1] Vasileios Paschalidis,[1,2] Thomas W. Baumgarte,[3] and Stuart L. Shapiro[4,5]
[1]*Department of Physics, University of Arizona, Tucson, Arizona 85721, USA*
[2]*Department of Astronomy, University of Arizona, Tucson, Arizona 85721, USA*
[3]*Department of Physics and Astronomy, Bowdoin College, Brunswick, Maine 04011, USA*
[4]*Department of Physics, University of Illinois at Urbana-Champaign, Urbana, Illinois 61801, USA*
[5]*Department of Astronomy and NCSA, University of Illinois at Urbana-Champaign, Urbana, Illinois 61801, USA*

(Received 19 June 2019; published 16 August 2019)

We investigate the dynamical stability of relativistic, differentially rotating, quasitoroidal models of neutron stars through hydrodynamical simulations in full general relativity. We find that all quasitoroidal configurations studied in this work are dynamically unstable against the growth of nonaxisymmetric modes. Both one-arm and bar mode instabilities grow during their evolution. We find that very high rest mass configurations collapse to form black holes. Our calculations suggest that configurations whose rest mass is less than the binary neutron star threshold mass for prompt collapse to black hole transition dynamically to spheroidal, differentially rotating stars that are dynamically stable, but secularly unstable. Our study shows that the existence of extreme quasitoroidal neutron star equilibrium solutions does not imply that long-lived binary neutron star merger remnants can be much more massive than previously found. Finally, we find models that are initially supra-Kerr ($J/M^2 > 1$) and undergo catastrophic collapse on a dynamical timescale, in contrast to what was found in earlier works. However, cosmic censorship is respected in all of our cases. Our work explicitly demonstrates that exceeding the Kerr bound in rotating neutron star models does not imply dynamical stability.

DOI: 10.1103/PhysRevD.100.043014

I. INTRODUCTION

Following the first ever multimessenger detection with gravitational waves (GWs) of a binary neutron star (BNS) [1], there have been a number of studies considering the stability of the merger remnant to place constraints on the nuclear equation of state [2–7]. The exact nature of the merger remnant is unknown, but it is possible that the remnant was a hypermassive neutron star (HMNS) [8–11]. HMNSs are differentially rotating stars with rest mass greater than that allowed by uniform rotation [12] (i.e., the supramassive limit [13]). The solution space of differentially rotating neutron stars has been studied in great detail for polytropes of varying polytropic indexes [14–16] (see also [17] for a review), and recently for realistic nuclear equations of state (EOSs) [18], strange quark star EOSs [19,20], and hybrid hadron-quark EOSs [21]. The solution space of differentially rotating neutron stars in equilibrium includes configurations that can support more than twice the maximum supportable rest mass by a nonrotating model with the same EOS, i.e., the Tolman-Oppenheimer-Volkoff (TOV) limit. There are even models that can support more than twice the supramassive limit mass with the same EOS. Such stars are highly unlikely to form following BNS mergers [18]. These extreme, differentially rotating configurations tend to be quasitoroidal, i.e., equilibria where the maximum energy (or rest mass) density of the fluid does not occur at the center of mass of the configuration but in a ring around it. Quasitoroidal configurations have so far been found only when differential rotation is allowed.

Differentially rotating massive neutron stars naturally arise as remnants of BNS mergers. Recent numerical simulations have shown that quasitoroidal HMNSs can form following a BNS merger [22,23]. There are also simulations that find a double core structure (see, e.g., [24,25,10] for a review on different types of BNS merger remnants). Despite this possibility, most relativistic simulations of isolated stars modeling BNS merger remnants have focused on spheroidal configurations (see [17] for a review). Dynamical simulations of HMNSs suggest that specific features can arise during the evolution, such as the one-arm instability [26–32], other nonaxisymmetric instabilities [33], the bar mode instability [12,34], and the low-$T/|W|$ instability [28,30,35–40]. Recent work has also considered the dynamical stability of differentially rotating, spheroidal stars based on approximate turning points [41,42]. Knowing whether such HMNSs are dynamically stable or unstable can inform us about the most massive remnants that may form following a BNS merger, how long such remnants may live for, the properties of the black hole

(BH) that forms when they collapse, and the subsequent electromagnetic signatures that accompany the GWs. Isolated stars can also help probe theoretical aspects of gravitation such as cosmic censorship and the ergoregion instability (see, e.g., [43–46]).

In this paper we examine the dynamical stability of quasitoroidal, differentially rotating neutron stars modeled as $\Gamma = 2$ polytropes. In [15,16] differentially rotating models that can support up to 4 times the TOV limit rest mass were found. In fact, there exists a continuum of quasitoroidal configurations that can support a range of masses. The reference mass in our study is the BNS threshold mass for prompt collapse to BH, which is 1.3–1.7 times the TOV limit mass [47–51] depending on the equation of state (note that the threshold mass refers to the premerger binary total rest mass). We consider equilibrium configurations that are above and below this threshold. Based on the fact that such high-mass equilibrium configurations exist, one might assume that long-lived BNS merger remnants much more massive than the BNS threshold mass for prompt collapse could possibly arise. Most of these extremely massive differentially rotating configurations are highly quasitoroidal, and their dynamical stability has never been tested before. If extreme quasitoroidal configurations are viable long-lived BNS merger remnants, they should be stable on a dynamical timescale.

Here we initiate a study of the dynamical stability of several quasitoroidal configurations that have rest masses ranging from astrophysically relevant values (∼1.4 times the TOV limit rest mass) to extreme, likely astrophysically irrelevant values (∼4.0 times the TOV limit rest mass). We perform hydrodynamic simulations in full $3+1$ general relativity of these configurations and find that all quasitoroidal configurations we investigate are dynamically unstable against the development of nonaxisymmetric modes. Both a one-arm and a bar mode grow during the evolution. We find that BH formation on a dynamical timescale is the outcome of configurations (quasitoroidal or spheroidal) with rest mass exceeding the BNS threshold mass for prompt collapse to BHs. On the other hand, one of our quasitoroidal configurations with rest mass less than the BNS threshold mass for prompt collapse transitions dynamically to a differentially rotating, *spheroidal* configuration that is dynamically stable, but secularly unstable.

Our work shows that the existence of the massive, extreme quasitoroidal neutron star solutions that were recently found in the literature do not imply that dynamically stable BNS merger remnants can exist with masses much larger than the BNS threshold mass for prompt collapse to a BH. Finally, several of the models we study are initially supra-Kerr ($J/M^2 > 1$), yet they undergo catastrophic collapse on a dynamical timescale. This result is in contrast to what was found in earlier work [52], where dynamically unstable, differentially rotating supra-Kerr models of $\Gamma = 2$ neutron stars could not be found, and supra-Kerr models could only be induced to collapse through severe pressure depletion. However, cosmic censorship is respected in all of our cases. Our study explicitly shows that exceeding the Kerr bound initially does not imply dynamical stability of a rotating neutron star configuration.

The rest of the paper is structured as follows. In Sec. II, we review the properties of the solution space of differentially rotating stars, and detail the properties of the equilibrium configurations we adopt as initial data for our simulations. In Sec. III, we briefly describe the set of initial perturbations we consider, our evolution code, and the diagnostics we employ in our analysis. In Sec. IV we describe the results of our simulations. In Sec. V we discuss our findings in connection with key global properties of the initial configurations and the final state of our quasitoroidal configuration that does not collapse to a BH. In Sec. VI we present out conclusions and discuss possible future avenues of investigation. Throughout this paper we adopt geometrized units, where $c = G = 1$ (where c is the speed of light in vacuum and G the gravitational constant). We commonly designate the TOV limit rest mass as $M_{0,\max}^{\rm TOV}$ and the gravitational [or Arnowitt-Deser-Misner mass (ADM)] mass as M.

II. SOLUTION SPACE OF DIFFERENTIALLY ROTATING STARS AND INITIAL EQUILIBRIA

The spacetime of stationary, axisymmetric, rotating neutron star equilibria is described in spherical polar coordinates r and θ by the line element [53] (see also [17] for a review of other line elements used in the literature),

$$ds^2 = -e^{\gamma+\rho}dt^2 + e^{2\alpha}(dr^2 + r^2 d\theta^2) + e^{\gamma-\rho} r^2 \sin^2\theta (d\phi - \omega dt)^2, \quad (1)$$

where $\gamma(r,\theta), \rho(r,\theta), \alpha(r,\theta)$, and $\omega(r,\theta)$ are the metric potentials determined by the solution of the Einstein equations coupled to the equation of hydrostationary equilibrium for perfect fluids. The matter is modeled as a perfect fluid whose stress-energy tensor is given by

$$T^{ab} = \rho_0 h u^a u^b + p g^{ab}, \quad (2)$$

where u^a, ρ_0, and p are the fluid four velocity, rest mass density, and pressure, respectively; h is the specific enthalpy, given by

$$h = 1 + \epsilon + \frac{p}{\rho_0}, \quad (3)$$

with ϵ the specific internal energy. To close the system of equations an EOS must be supplied. In this work we focus on polytropic EOSs which are described by

$$p = \kappa \rho_0^{\Gamma}, \tag{4}$$

where κ is the polytropic constant and Γ is the adiabatic index. In particular, we consider stars that are described by $\Gamma = 2$. We also adopt polytropic units (equivalent to setting $\kappa = 1$) unless otherwise noted.

The integrability condition on the equation of hydrostationary equilibrium enforces that the specific angular momentum ($j = u^t u_\phi$) be a function of the angular velocity Ω as measured by an observer at infinity at rest, i.e., $j = u^t u_\phi = F(\Omega)$. By choosing $F(\Omega)$, we specify a rotation law for the matter. Here we work with the Komatsu-Eriguchi-Hachisu (KEH) rotation law [54],

$$F(\Omega) = A^2(\Omega_c - \Omega), \tag{5}$$

where Ω_c is the angular velocity at the pole. The parameter A in Eq. (5) has units of length and parametrizes the length scale over which the angular velocity changes in the star. As in previous studies, we work with a rescaled version of A given by

$$\hat{A}^{-1} = \frac{r_e}{A}, \tag{6}$$

where r_e is the equatorial radius of the configuration. The parameter $\hat{A}^{-1}$ (which we refer to as the degree of differential rotation) lies in the range $0 \leq \hat{A}^{-1} < \infty$, with $\hat{A}^{-1} = 0$ corresponding to uniform rotation.

Under the assumption of the KEH rotation law, it was shown in [14–16] that the solution space of differentially rotating, polytropic neutron stars can generally be divided into four classes. It was recently also shown that at least three of these classes also exist for realistic EOSs [18] and for hybrid EOSs [21]. Each solution type may be characterized by specific ranges of the values in the quadruplet $(\epsilon_{\max}, r_p/r_e, \hat{A}^{-1}, \hat{\beta})$, where $\epsilon_{\max}$ is the maximum energy density in the star, r_p/r_e is the ratio of polar to equatorial radius (which parametrizes the angular velocity at the center of the star), and $\hat{\beta}$ is the mass-shedding parameter which measures how close to the Keplerian limit the configuration is. The parameter $\hat{\beta}$ is defined as [14]

$$\hat{\beta} = \frac{\beta}{1+\beta}, \tag{7}$$

where

$$\beta = -\left(\frac{r_e}{r_p}\right)^2 \left.\frac{\mathrm{d}(z_b^2)}{\mathrm{d}(\varpi^2)}\right|_{\varpi = r_e}, \tag{8}$$

with $\varpi = r\sin(\theta)$ and $z = r\cos(\theta)$ the usual cylindrical coordinates, and $z = z_b$ describing the surface of the star. The mass-shedding parameter takes on several limiting values depending on the shape of the configuration. Configurations at the mass-shedding limit have $\mathrm{d}(z_b^2)/\mathrm{d}(\varpi^2)|_{\varpi=r_e} = 0$ and hence $\hat{\beta} = 0$; spherical (nonrotating) models correspond to $r_p/r_e = 1$, $\mathrm{d}(z_b^2)/\mathrm{d}(\varpi^2)|_{\varpi=r_e} = -1$, and hence $\hat{\beta} = \frac{1}{2}$; quasitoroids correspond to $r_p/r_e \to 0$, and $\hat{\beta} \to 1$. In this work we focus on configurations with small but nonzero values of r_p/r_e, which are the quasitoroids.

In Fig. 1 we show a projection of the solution space for a $\Gamma = 2$ polytrope in the $(\hat{\beta}, r_p/r_e)$ plane at a fixed value of $\epsilon_{\max}$. The methods we adopt for building these stars are the same as those developed in [18]. The different lines in Fig. 1 correspond to sequences of constant $\hat{A}^{-1}$ [or contours of the function $\hat{A}^{-1}(\hat{\beta}, r_p/r_e)$]. Each curve is labeled by its corresponding value of $\hat{A}^{-1}$. The solid black line corresponds to the critical degree of differential rotation $\hat{A}^{-1}_{\mathrm{crit}}$ which divides the solution space into four regions, each corresponding to one of the four solution types. In this study we will focus on the solution types that we were able to build with the code of Cook *et al.* [13,53,55], namely the type A, B, and C solutions detailed in [14]. Since we were unable to construct type D models, the $\hat{A}^{-1}_{\mathrm{crit}}$ curve divides the plot in Fig. 1 into only three regions (see Fig. 2 in [14] for an example of the complete solution space for a $\Gamma = 2$ polytrope with $\epsilon_{\max} = 0.12$). The type A solutions consist

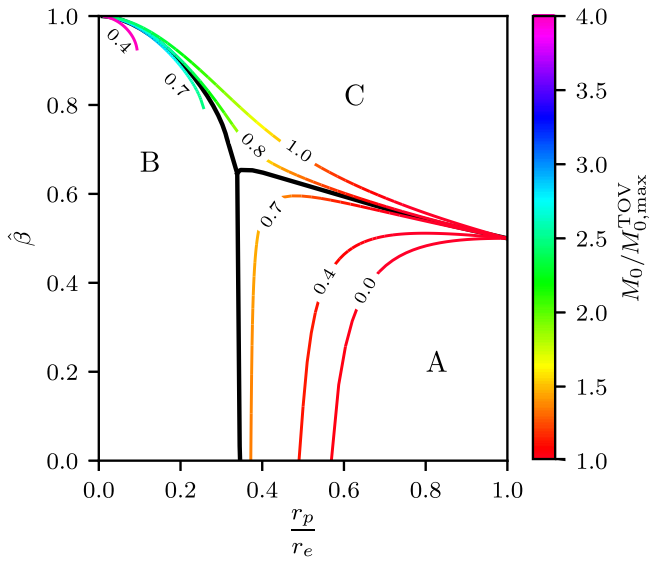

FIG. 1. Projection of the solution space for a $\Gamma = 2$ polytrope in the $(r_p/r_e, \hat{\beta})$ plane for a fixed value of the stellar maximum energy density $\epsilon_{\max} = 0.12$ (in polytropic units) and several values of the degree of differential rotation $\hat{A}^{-1}$. Each sequence is labeled by $\hat{A}^{-1}$. The bold black line corresponds to the critical value of the degree of differential rotation $\hat{A}^{-1}_{\mathrm{crit}} = 0.75904$ [14], which here divides the solution space into three regions corresponding to type A (bottom right), B (left), and C (top) models. The color bar corresponds to the rest mass of models along each sequence of fixed $\hat{A}^{-1}$, normalized by the maximum rest mass for a nonrotating model (i.e., the TOV limit rest mass) $M_{0,\max}^{\mathrm{TOV}}$.

TABLE I. Properties of the equilibrium models considered in this work. For each model we list the model label/model type, the dimensionless spin parameter J/M^2, the central period divided by the ADM mass T_c/M, the rest mass M_0 in units of $M^{\rm TOV}_{0,\rm max}$ (the TOV limit rest mass), the ADM mass M in units of $M^{\rm TOV}_{\rm max}$ (the TOV limit gravitational mass), the compactness $C = M/R_c$ (with R_c the circumferential radius at the equator), the ratio of kinetic to gravitational potential energy $T/|W|$, the maximum energy density $\epsilon_{\rm max}$ in units of $\epsilon^{\rm TOV}_{\rm max}$ (the maximum energy density of the TOV limit configuration), the ratio of polar to equatorial radius r_p/r_e, the degree of differential rotation $\hat{A}^{-1}$, and the mass-shedding parameter $\hat{\beta}$.

Model	J/M^2	T_c/M	$M_0/M^{\rm TOV}_{0,\rm max}$	$M/M^{\rm TOV}_{\rm max}$	C	$T/\lvert W\rvert$	$\epsilon_{\rm max}/\epsilon^{\rm TOV}_{\rm max}$	r_p/r_e	$\hat{A}^{-1}$	$\hat{\beta}$
A	0.89	27.95	1.63	1.66	0.22	0.22	0.74	0.35	0.7	0.66
B	1.07	24.78	3.79	3.73	0.28	0.33	0.21	0.035	0.4	0.99
C	1.02	21.97	2.57	2.59	0.25	0.29	0.23	0.005	0.8	0.99
$B_{\rm low}$	1.56	144.67	1.36	1.47	0.09	0.3	0.05	0.005	0.8	0.99
$C_{\rm low}$	0.89	15.38	1.81	1.85	0.23	0.24	0.29	0.01	1.5	0.99

of spheroidal models and correspond to relatively low degrees of differential rotation $\hat{A}^{-1} < \hat{A}^{-1}_{\rm crit}$. Spinning these stars up, i.e., decreasing r_p/r_e, results in mass shedding. Type A solutions reside in the lower right part of Fig. 1, where one end of the sequences is located at $\hat{\beta} = 0.5$ (corresponding to a spherical model) and the other is located at $\hat{\beta} = 0$ (corresponding to mass shedding). Type B solutions are related to type A models, in that they may exist for the same values of $\hat{A}^{-1} < \hat{A}^{-1}_{\rm crit}$, but they are quasitoroidal. The type B solutions correspond to the left side of Fig. 1; these sequences have one end located at $\hat{\beta} = 1$ (corresponding to a toroidal model) and the other located at $\hat{\beta} = 0$ (corresponding to mass shedding). We were unable to construct type B stars pinched at the equator, which results in type B sequences shown in Fig. 1 that do not terminate at the mass-shedding limit. Type B solutions are the most massive among the four types, as also depicted by the color bar in Fig. 1. The type C sequences include both spheroidal and quasitoroidal models. Nevertheless, the most massive models in this class of stars tend to be extremely close to a toroidal topology. The fourth solution class, type D, is also quasitoroidal (see [14] for more details). For each of the solution types considered, we built the maximum rest mass models found in [14].

We searched the solution space for the maximum rest mass models by building sequences of solutions at constant $\epsilon_{\rm max}$ as detailed in [18]. We present relevant properties of these maximum rest mass models in Table I. For the two quasitoroidal solution types, we also consider lower mass equilibria (labeled $B_{\rm low}$ and $C_{\rm low}$) to probe the role that the rest mass plays on stability. As shown in Table I the maximum mass type B models are the most massive ones supporting up to 4 times the TOV limit rest mass. Equatorial contours of the rest mass density of the most massive A, B, and C type models in Table I are shown in Fig. 2. Figure 2 shows the quasitoroidal nature of the B and C models, where an underdense region exists at the geometric center of the configuration, and the maximum rest mass density is located in a ring around the center. These models, along with the $B_{\rm low}$ and $C_{\rm low}$ models listed in Table I, represent our initial equilibria.

III. METHODS

We evolve the initial data presented in Sec. II using the well-tested Illinois GRMHD code [56,57] which operates

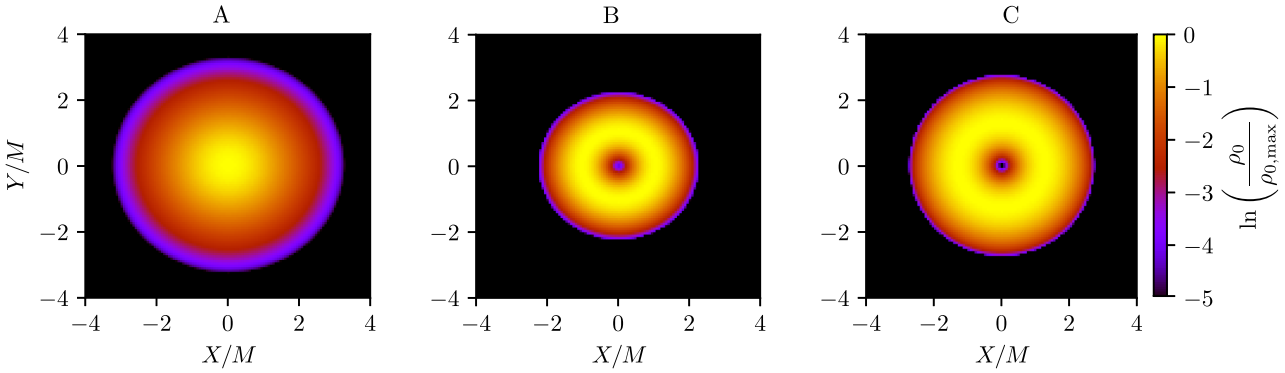

FIG. 2. Equatorial contours (i.e., on the X-Y plane, where we scale the X and Y coordinate by the gravitational mass M) of the rest mass density ρ_0 at $t = 0$ for the maximum rest mass A, B, and C type models (left, middle, and right, respectively) in Table I. The color bar shows the value of the rest mass density scaled to the maximum value on a logarithmic scale.

within the CACTUS infrastructure [58] and uses CARPET [59,60] for mesh refinement. Illinois GRMHD solves the Einstein equations within the ADM $3+1$ framework and evolves the spacetime using the Baumgarte-Shapiro-Shibata-Nakamura (BSSN) formulation of the Einstein equations [61,62]. Our gauge choice employs 1+log time slicing for the lapse [63] and the "Gamma-freezing" condition for the shift cast in first order form [64,65] [see also Eqs. (2)–(4) in [66]]. We use the MoL thorn to solve the equations in time by the use of a fourth order Runge-Kutta scheme with the Courant factor set to 0.5. We ignore magnetic fields, and the equations of hydrodynamics are solved in conservation-law form adopting the high-resolution shock-capturing methods described in [67,68]. To close the evolution system, an EOS needs to be provided. We adopt a Γ-law EOS $P = (\Gamma - 1)\rho_0\epsilon$, with $\Gamma = 2$, for the evolution.

A. Grid hierarchy

Our fixed mesh refinement grid hierarchy consists of nested cubes with seven refinement levels. The finest level half-side length is set to $r_1 \approx 1.25R_{\rm NS}$, where $R_{\rm NS}$ is the neutron star coordinate equatorial radius. Thus, the entire star is covered by the finest level. The half-side length of refinement level n is set to $r_n = 2^{(n-1)}r_1$ (where $n = 1$ corresponds to the finest level and $n = 7$ to the coarsest one). We set the spatial resolution on the finest level to $dx_1 = M/20$ in order to capture BH properties should a BH form following collapse of the star, where M is the ADM mass of the initial configuration. Each subsequent refinement level has half the resolution of the previous. Therefore, the resolution of refinement level n is given by $dx_n = 2^{(n-1)}dx_1$. Cartesian coordinates are adopted, and equal resolution is chosen for the x, y, and z directions. We impose reflection symmetry across the equatorial plane to reduce computational cost, such that our grid extent in the z direction is $0 \le z \le 80R_{\rm NS}$. We do not impose a π-rotational symmetry, so that odd-number nonaxisymmetric modes are not artificially suppressed [69]. In the type A and type B cases we also performed simulations at 1.2 times and 1.5 times the canonical resolution. The code of Cook *et al.* uses spherical coordinates, whereas Illinois GRMHD uses Cartesian coordinates. To avoid coordinate singularities in transforming the initial data from spherical to Cartesian coordinates we shift our Cartesian coordinates in the y direction by a small amount to avoid the origin of the coordinate system. In the Appendix we investigate the effects of grid resolution and the y-coordinate shift on our results.

B. Initial perturbations

Each of the initial configurations presented in Table I is evolved without and with initial perturbations. We consider three types of perturbations: (a) we evolve the initial data after exciting a quasiradial perturbation in the star. We achieve this by locally depleting the pressure by 0.5% everywhere in the star at $t = 0$; we also excite (b) one-arm ($m = 1$) and (c) bar mode ($m = 2$) nonaxisymmetric rest mass density perturbations of the form [70]

$$\rho_0 \to \rho_0\left(1 + \frac{B\varpi\sin(m\phi)}{r_e}\right), \tag{9}$$

where r_e is the stellar coordinate equatorial radius, ϕ is the azimuthal coordinate, and B is the perturbation amplitude. We excite only one perturbation per evolution to determine the role that each mode plays. Given that we have five configurations in Table I and four types of evolutions, we have a total of 20 cases in our study. In all of the evolutions considered, we set $B = 0.5\%$. Note that 0.5% is the maximum perturbation near the edge of the star. Near the location of the maximum density this is reduced to $\sim$0.1%. We have checked that the amplitude of our initial perturbations is small enough that truncation error dominates the initial constraint violations. Therefore, we do not resolve the constraints after applying the perturbation.

C. Diagnostics

We use several diagnostics during the evolution to test for stability against collapse, assess nonaxisymmetric mode growth, measure black hole properties, and extract GWs. We calculate the maximum of the rest mass density as a function of time $\rho_{0,\rm max}(t)$ to determine whether the configuration is undergoing collapse. The "collapse" of the lapse function is also used as an indicator for BH formation. We locate BH apparent horizons (AH) with the AHFINDERDIRECT thorn [71]. The AHFINDERDIRECT thorn provides the BH irreducible mass as well as the equatorial and meridional AH circumferences. The ratio C_r of the meridional circumference to that of the equator can be used to provide a good approximation to the BH dimensionless spin, for which we employ the approximating formula of [72]

$$a_{\rm BH} = \sqrt{1 - (2.55C_r - 1.55)^2}. \tag{10}$$

This formula is derived for a Kerr spacetime and is applicable to the final black hole as the spacetime approaches the Kerr solution at late times.

We compute the volume-integrated azimuthal density mode decomposition, given by [22,69,73]

$$C_m = \int \sqrt{-g}\rho_0 u^0 e^{im\phi} d^3x, \tag{11}$$

to test for the growth of nonaxisymmetric modes. Note that C_0 is the total rest mass of the configuration. Note also that Eq. (11) yields zero for $|m| > 0$, if the density, velocity, and metric fields are axisymmetric.

Equation (11) is useful for a qualitative understanding of the matter evolution, but does not provide a gauge-invariant measure of nonaxisymmetric modes. Therefore, we also extract gravitational radiation to determine the growth of nonaxisymmetric modes during the evolution. For this, we compute the Newman-Penrose scalar Ψ_4 and decompose it into $s=-2$ spin-weighted spherical harmonics, to determine the growth of axisymmetric ($m=0$) and nonaxisymmetric ($m\neq 0$) GW modes during evolution in a gauge-invariant way. We denote the coefficients of this decomposition as $\Psi_4^{l,m}$ and focus on the $l=2$, $m=0$, $m=1$, and $m=2$ modes in this work. We compute $|\Psi_4^{2,m}|$ in the wave zone. We find that generally C_m and $\Psi_4^{2,m}$ are consistent as indicators of nonaxisymmetric mode growth, i.e., the same nonaxisymmetric modes that are excited in C_m are also excited in $\Psi_4^{2,m}$. This is not unexpected because the decomposition in both diagnostics carries the $e^{im\phi}$ term. We show these diagnostics in Sec. IV.

Finally, we also monitor the L_2 norm of the Hamiltonian $||\mathcal{H}||$ and momentum $||\mathcal{M}||$ constraints via Eqs. (40) and (41) in [66], which along with Ψ_4 we use to demonstrate convergence in Appendix.

IV. RESULTS

In this section we present the results from dynamical spacetime simulations of the models listed in Table I under no initial perturbation and the three types of initial perturbations we described in Sec. III B. For each model we scale the evolution time by the initial period at the center of the configuration T_c, all rest mass densities by the maximum at the start of simulation $\rho_{0,\max}(0)$, and all density mode amplitudes by the amplitude of the dominant C_0 mode. We generally find that the quasitoroidal models considered here are unstable to nonaxisymmetric mode growth on dynamical timescales. First, we discuss our study of the most massive models, and subsequently we present the results from the lower-mass models.

A. Most massive A, B, C models

Here we report our results for the most massive A, B, and C models listed in Table I, categorized by the type of perturbation considered at the start of simulation.

1. Evolution of equilibrium configurations without perturbation

When evolving the initial equilibria without perturbation, we find that all models except for model A are unstable to the growth of nonaxisymmetric modes on a dynamical timescale. We will often refer to evolutions without initial perturbation as "equilibrium evolutions."

In the left panel of Fig. 3 we show the maximum rest mass density $\rho_{0,\max}$ as a function of time. We show the evolution either up to collapse (for models which form BHs) or until an approximately steady state has been reached (for noncollapsing models). Figure 3 shows that the equilibrium evolution of the A model results in a ∼10% oscillation of the maximum rest mass density about the value $\rho_{0,\max}/\rho_{0,\max}(0)\approx 0.87$. In this case, we evolved the A model until $t\approx 10T_c$ and saw no sign of dynamically unstable mode growth by the end of simulation. However, together with the fact that this model is unstable to radial perturbations (as discussed in the next subsection), the oscillation of $\rho_{0,\max}$ by ∼10% suggests that this model is only marginally stable. By contrast, in models B and C the density grows slowly until it reaches a point after which it increases rapidly and the configurations undergo catastrophic collapse.

Although we do not excite any perturbations, seeded perturbations at the level of truncation error grow such that all quasitoroidal models exhibit nonaxisymmetric instabilities. This can be seen in the center and right panels of

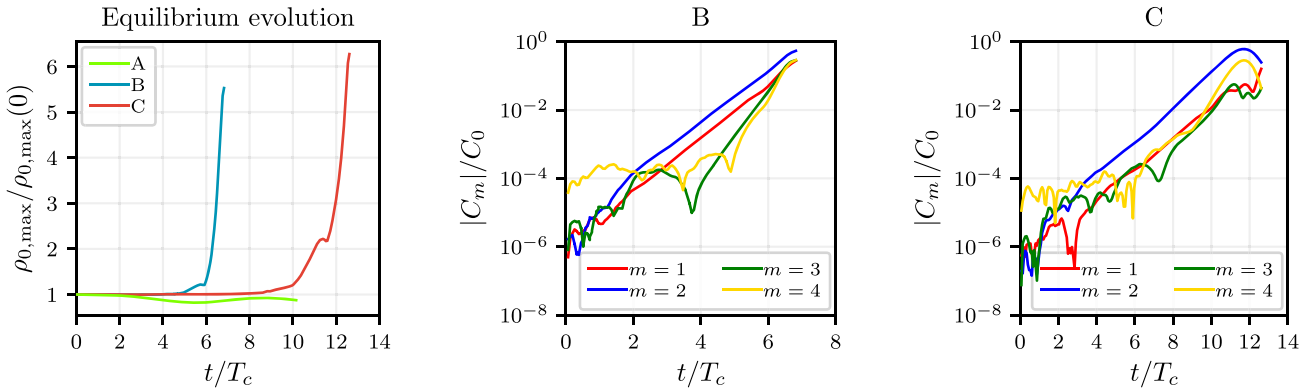

FIG. 3. Left panel: Maximum rest mass density as a function of time for the A, B, and C models in the case of zero initial perturbations. The green, blue, and red lines correspond to the A, B, and C models, respectively. Center panel: Evolution of the amplitude $|C_m|$ of nonaxisymmetric density modes for the B model [$m=1$(red line), $m=2$(blue line), $m=3$(green line), and $m=4$(yellow line)] in the case of zero initial perturbations. Right panel: Same as the center panel but for the C model.

Fig. 3, where we show the azimuthal density mode decomposition, with mode amplitudes given by Eq. (11). We focus on the $m = 1, 2, 3$, and 4 modes. We find that the $m = 1$ and $m = 2$ modes grow at similar rates (exponentially with time) dominating over the higher modes. Nevertheless, the $m = 2$ mode is dominant throughout most of the evolution for the quasitoroidal models. Model A does not exhibit any growth of nonaxisymmetric modes and is not plotted here. We find that the B and C configurations are especially unstable to nonaxisymmetric modes corresponding to the bar mode instability, even though the $m = 2$ mode was not explicitly excited at the start of simulation. The evolution of the cases developing strong $m = 2$ modes generally proceeds as in the dynamical bar mode instability [12,34,74], but eventually leads to catastrophic collapse.

In Fig. 4 we show density contours on the equatorial plane that demonstrate how the dynamics of a strong $m = 2$ mode proceeds in the C model under equilibrium evolution. First, two overdense regions develop in the ring of maximum density of the quasitoroids (left panel of Fig. 4). Next, as the two overdense regions move apart, a typical high-density bar develops, with the two overdense regions forming the "arms" of the bar (center panel of Fig. 4). As the two overdense arms coalesce near the geometric center of the configuration, the maximum rest mass density in the bar continues to rise. For the most massive models, such as the B and C models, the maximum density grows rapidly until complete gravitational collapse ensues and a single BH forms near the center of mass (right panel of Fig. 4).

The value of $\rho_{0,\max}(t)$ also shows features which are consistent with a dominant $m = 2$ mode in cases that develop $m = 2$ nonaxisymmetries in our study. As shown in the left panel of Fig. 3, $\rho_{0,\max}$ shows a local peak prior to collapse (the local peak is seen at $t \approx 5.75T_c$ for the B model and $t \approx 11T_c$ for the C model). This local maximum in time coincides with the saturation of the bar as it reaches maximum density. After this brief saturation, the two overdense arms of the bar mode bounce, launching shocks which lead to a momentary decrease in $\rho_{0,\max}$ that explains the "dip" in the evolution of the maximum rest mass density. Eventually, the overdense arms coalesce near the geometric center, leading to a significant rise in $\rho_{0,\max}$, and ultimately to catastrophic collapse. This "double-peak" feature is observed in many of our cases with a dominant $m = 2$ mode.

2. Pressure depletion

In the left panel of Fig. 5 we show the evolution of the maximum rest mass density and the density mode decomposition in the case of pressure depletion for the most massive models. The evolution of the maximum rest mass density is comparable to the case of equilibrium evolution for the quasitoroidal B and C models, and they collapse practically on the same timescales as in the evolution without perturbation. This suggests that these stars are not quasiradially unstable, but are unstable only to the development of nonaxisymmetric modes.

The quasiradial ($m = 0$) pressure depletion evolution was the only type of evolution that resulted in collapse for the A model, which indicates that on dynamical timescales it is unstable to collapse against quasiradial perturbations, but not against nonaxisymmetric ones. Note that model A has a rest mass of $M_0^{\rm A} = 1.8 M_{0,\max}^{\rm TOV}$, and the fact that it collapses to a BH following a quasiradial perturbation is coincidentally consistent with the threshold mass of 1.65–$1.75 M_{0,\max}^{\rm TOV}$ for prompt collapse in the case of $\Gamma = 2$ BNS mergers [47].

Compared to the equilibrium evolutions, in the case of pressure depletion we observe a stronger $m = 1$ density mode developing early in the evolution of the most massive quasitoroids, with the $m = 1$ density mode comparable to

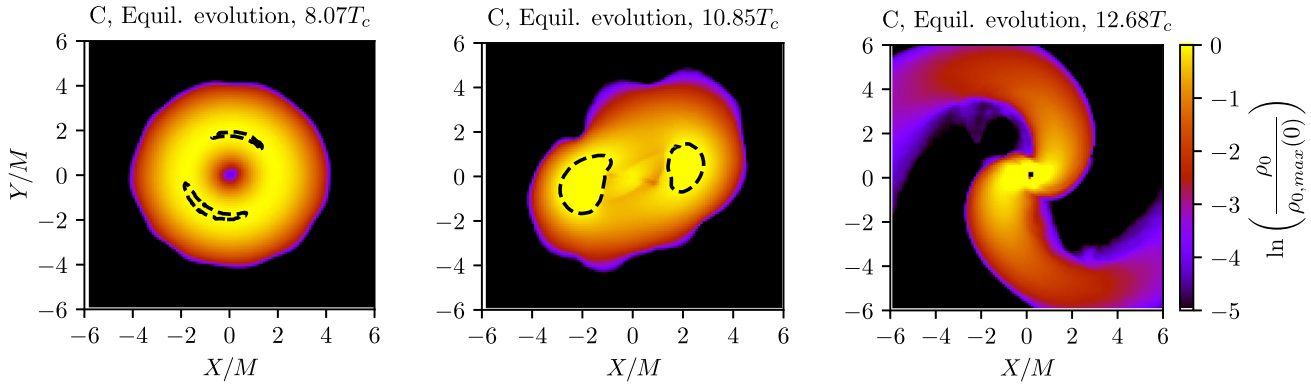

FIG. 4. Snapshots of equatorial contours (i.e., on the X-Y plane) of the rest mass density ρ_0, scaled to the maximum value at the start of simulation $\rho_{0,\max}(0)$ for the C model under equilibrium evolution. The dashed lines indicate the boundary of the regions within which the rest mass density satisfies $\rho_0 \geq \rho_{0,\max}(0)$. The left and center panels show the development of the model at $t = 8.07T_c$ and $t = 10.85T_c$, respectively. The right panel shows the state of the model in the time near collapse at $t = 12.68T_c$.

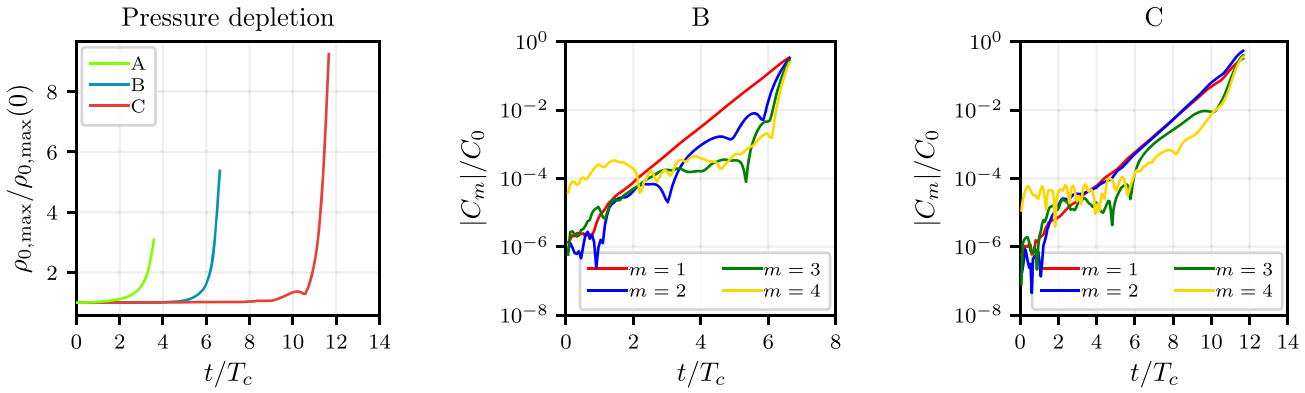

FIG. 5. Same as Fig. 3 but for the case of pressure depletion.

the $m = 2$ mode in the time leading up to collapse or by the end of simulation. The evolution in the case where an $m = 1$ density mode dominates in quasitoroids generally proceeds as follows: first, a single overdense region develops somewhere in the ring of maximum rest mass density in the quasitoroid. Next, this single overdense region develops a single arm, akin to the one-arm instability [26,27]. For massive enough configurations, the overdense region continues to collapse until it forms a BH.

The similarity in amplitude and growth times for the $m=1$ and $m = 2$ density modes in the cases of equilibrium and pressure depletion evolutions of the quasitoroidal models suggests that whichever mode is excited first, and with stronger amplitude, will dominate throughout the evolution. We test this expectation in the following subsection.

3. Nonaxisymmetric perturbations

Under nonaxisymmetric initial perturbations, the A model did not collapse and evolved in a fashion similar to the equilibrium evolution case [see the left panel of Fig. 6, where we show the value of $\rho_{0,\max}(t)$ for the A, B, and C models under both $m = 1$ (solid lines) and $m = 2$ (dash-dotted lines) initial perturbations]. Thus, we focus the discussion on the quasitoroidal models here.

In the cases discussed thus far, the dominant density modes during evolution have been the $m = 1$ and $m = 2$ modes. To better understand the features of evolution in the case of strong nonaxisymmetric mode growth, we excite initial perturbations of the form given in Eq. (9) with $m = 1$ or $m = 2$. We find that the $m = 1$ and $m = 2$ density modes grow on very similar timescales for both the B and the C models, with the $m = 1$ initial perturbation forcing slightly earlier collapse than the $m = 2$ initial perturbation (see the left panel of Fig. 6).

In the center and right panels of Fig. 6 we show the density mode decomposition for the B (solid lines) and C (dashed lines) models in the case of $m = 1$ and $m = 2$ initial perturbations, respectively. We focus on the evolution of the two most dominant density modes ($m = 1$ in red and $m = 2$ in blue). Exciting an $m = 1$ or $m = 2$ mode at the start of simulation ensures that the corresponding mode is dominant throughout the evolution. We observe that in

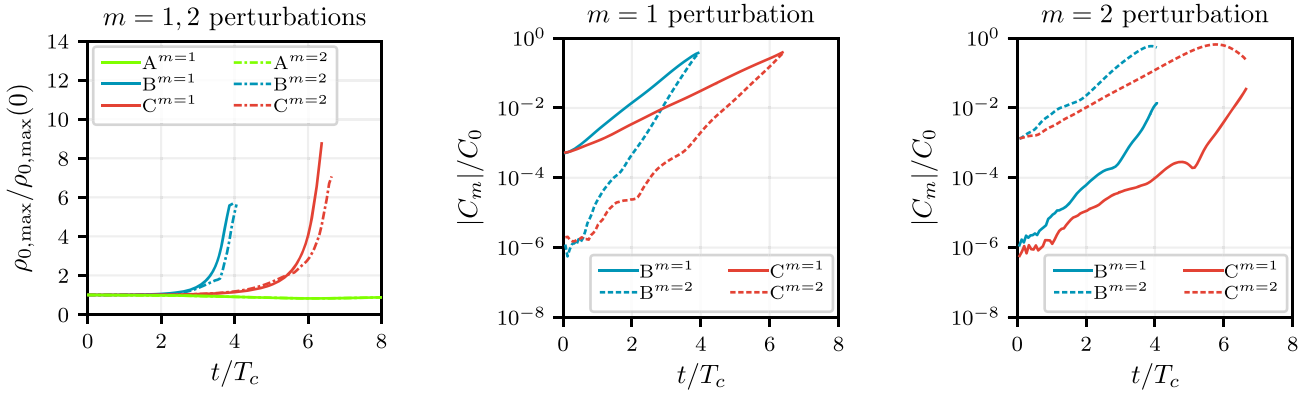

FIG. 6. Left panel: Maximum rest mass density as a function of time for the A, B, and C models in the case of nonaxisymmetric $m = 1$ (solid lines) and $m = 2$ (dash-dotted lines) initial rest mass density perturbations. The green, blue, and red lines correspond to the A, B, and C models, respectively. Center panel: Evolution of the dominant $m = 1$ (solid lines) and $m = 2$ (dashed lines) nonaxisymmetric density modes for the B (blue lines) and C (red lines) models in the case of an $m = 1$ perturbation. Right panel: Same as the center panel but for an $m = 2$ perturbation.

the case where an $m = 1$ mode is initially explicitly excited, the amplitude of the $m = 2$ density mode becomes comparable to that of the $m = 1$ mode near collapse, but the $m = 1$ density mode remains dominant. In the case where an $m = 2$ mode is initially excited, the $m = 2$ density mode remains significantly stronger than the $m = 1$ mode even until collapse (e.g., compare the center and right panels of Fig. 6). On the other hand, exciting an $m = 1$ mode initially tends to lead to faster collapse.

These results show that the one-arm instability is as important as the bar mode instability in collapsing quasitoroidal configurations, and that the nonaxisymmetric mode, which dominates early in the evolution of an unstable quasitoroidal configuration, is chiefly responsible for its collapse.

B. Low mass B and C models

The most massive B and C models considered thus far have $M_{0,\max} > 2M^{\rm TOV}_{0,\max}$, making them unlikely models of BNS merger remnants. For this reason, we also consider the dynamical stability of models with a rest mass that could represent the total rest mass of BNSs. In this section we present our results for the low mass type B and C models (which we refer to as $\rm B_{low}$ and $\rm C_{low}$) listed in Table I to study the effect of total mass on the stability of quasitoroidal neutron stars.

1. Evolution of equilibrium configurations without perturbation

Model $\rm B_{low}$, which is the lowest rest mass quasitoroidal model in our study, undergoes nonaxisymmetric instabilities and transitions dynamically from a quasitoroidal shape to a spheroidal one. This dynamical transition was observed for all types of evolutions we considered. Here we describe the basic evolution of the configuration and its unstable modes, and we discuss the properties of the final state in Sec. V C.

In the left panel of Fig. 7 we plot $\rho_{0,\max}(t)$ for the equilibrium evolution of model $\rm B_{low}$. The maximum rest mass density peaks at $\rho_{0,\max} \approx 2.5\rho_{0,\max}(0)$ and subsequently oscillates around $\rho_{0,\max} \approx 1.7\rho_{0,\max}(0)$ as the configuration evolves toward a steady state. The fact that the maximum density does not continue to increase demonstrates that this configuration is dynamically stable against catastrophic collapse, but it will collapse on secular timescales due to viscous/magnetic effects that redistribute angular momentum, because the total rest mass exceeds the supramassive limit rest mass [75–77]. The presence of the dip in the maximum density evolution after its first peak is consistent with the feature discussed in IV A 1, where the bar mode dominates the evolution. Thus, the maximum density evolution alone suggests that the equilibrium evolution of model $\rm B_{low}$ develops a bar mode early on. This can be seen in the density mode decomposition, which is plotted in the center panel of Fig. 7 and shows the $m = 2$ mode dominance. The plateau, which the $m = 2$ density mode exhibits in the time interval $\sim$6–8T_c, corresponds to the saturation of the bar mode. The time of onset of the bar mode saturation coincides with the first peak of the maximum rest mass density. Subsequently, a single, approximately spheroidal, overdense region forms, giving rise to the second peak of the maximum rest mass density (seen at $t \approx 8T_c$ in the left panel of Fig. 7). The formation of the single spheroidal overdense region signals the decay of the $m = 2$ mode that starts at $t \approx 8T_c$ (center panel of Fig. 7).

Model $\rm C_{low}$ undergoes catastrophic collapse in the case of equilibrium evolution, which is indicated by the rapidly increasing maximum density in the left panel of

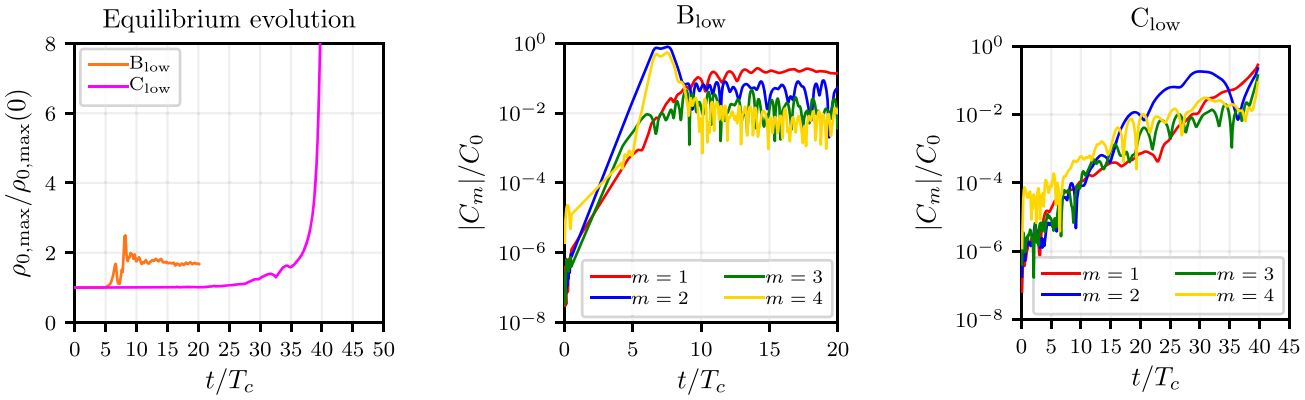

FIG. 7. Left panel: Maximum rest mass density as a function of time for the $\rm B_{low}$ and $\rm C_{low}$ models in the case of zero initial perturbations. The orange and magenta lines correspond to the $\rm B_{low}$ and $\rm C_{low}$ models, respectively. Center panel: Evolution of nonaxisymmetric density modes for the $\rm B_{low}$ model for the [$m = 1$(red line), $m = 2$(blue line), $m = 3$(green line), and $m = 4$(yellow line)] modes in the case of zero initial perturbations. Right panel: Same as the center panel but for the $\rm C_{low}$ model. Note that model $\rm B_{low}$ has a central period which in units of M is almost an order of magnitude longer than that of model $\rm C_{low}$. Thus, the evolution of model $\rm B_{low}$ is very long. It is the normalization with respect to T_c that makes it appear that this evolution is short.

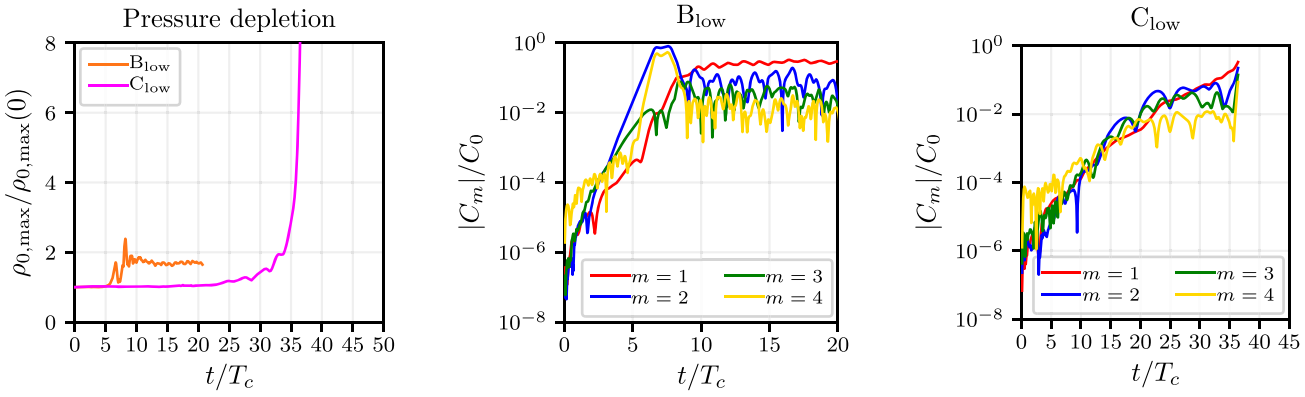

FIG. 8. Same as Fig. 7 but for the case of pressure depletion.

Fig. 7. Model C_{low} is unstable against the development of nonaxisymmetric modes as shown in the right panel of Fig. 7, which drive the evolution toward catastrophic collapse.

2. Pressure depletion

In Fig. 8 we show the evolution of the maximum rest mass density and the azimuthal density modes for the pressure depletion perturbation. These are practically the same as the equilibrium evolution for model B_{low} and very similar to the equilibrium evolution for model C_{low}. Only the dominant nonaxisymmetric density modes are slightly different, but qualitatively the evolutions are very similar. The dynamical transition to a spheroidal model for model B_{low} and the collapse for model C_{low} in this case occur practically on the same timescale as in the equilibrium evolution case. This is a clear indication that these quasitoroidal models are not unstable against quasiradial perturbations. As in the equilibrium evolution case, nonaxisymmetric modes seeded at the level of truncation error dominate the evolution.

3. Nonaxisymmetric perturbations

To test whether the initial excitation of an $m=1$ or $m=2$ mode leads to dominance of the excited nonaxisymmetric mode, we now consider $m = 1$ and $m = 2$ initial perturbations separately. Before discussing the evolution of azimuthal density modes in each case, we first discuss the general dynamics and how the evolution proceeds in the B_{low} model for nonaxisymmetric initial perturbations. The C_{low} model evolves similarly to the B_{low} model with a strong one-arm mode developing in the case of an $m = 1$ initial perturbation, and a strong bar mode developing in the case of an $m = 2$ initial perturbation, but ultimately leading to catastrophic collapse.

In Fig. 9 we show equatorial snapshots of the rest mass density for the B_{low} model in the cases of $m = 1$ and $m = 2$ perturbations. In the plots we also indicate with dashed lines the regions where $\rho_0 \geq \rho_{0,max}(0)$, which early on show where in the star the one-arm or bar modes begin to grow.

In the case of the $m = 1$ initial perturbation, first a single overdense region develops in the high-density ring around the center of mass (see the top left panel of Fig. 9). The growth of the $m = 1$ mode occurs on a dynamical timescale and the overdense region quickly grows (top center panel of Fig. 9), eventually migrating toward the geometric center of the original configuration and settling there (top right panel of Fig. 9).

When an $m=2$ perturbation is initially excited, the $m = 2$ mode is seen to dominate throughout the evolution. A bar develops early on, and the two arms of the bar continue to separate into a dumbbell-like configuration, with two overdense regions momentarily orbiting around a third overdense region near the center of mass (see the bottom left panel of Fig. 9). Subsequently, the bar mode saturates, after which the two overdense arms coalesce with the central overdense region to form a *single* overdense core (see the bottom center panel of Fig. 9). The configuration eventually settles toward a spheroidal shape (bottom right panel of Fig. 9).

In Fig. 10, we show the evolution of the maximum rest mass density and the density mode decomposition for the B_{low} and C_{low} models under initial nonaxisymmetric rest mass density perturbations. For the B_{low} model, at late times $\rho_{0,max}$ exhibits small oscillations around the value $\rho_{0,max} \approx 1.85\rho_{0,max}(0)$ for the $m = 1$ initial perturbation case, and at $\rho_{0,max} \approx 2\rho_{0,max}(0)$ in the $m = 2$ initial perturbation case. Note that in the cases of equilibrium evolution and pressure depletion the quasi–steady state maximum rest mass density is closer to $1.7\rho_{0,max}(0)$. This result suggests that the remnants may be settling to similar (though not identical) final configurations. We investigate this issue further in the next section. The center and right panels of Fig. 10 show only the dominant $m = 1$ and $m = 2$ density mode amplitudes. The plots demonstrate clearly that when an $m = 1$ ($m = 2$) mode is initially excited, then the $m = 1$ ($m = 2$) density mode dominates the evolution.

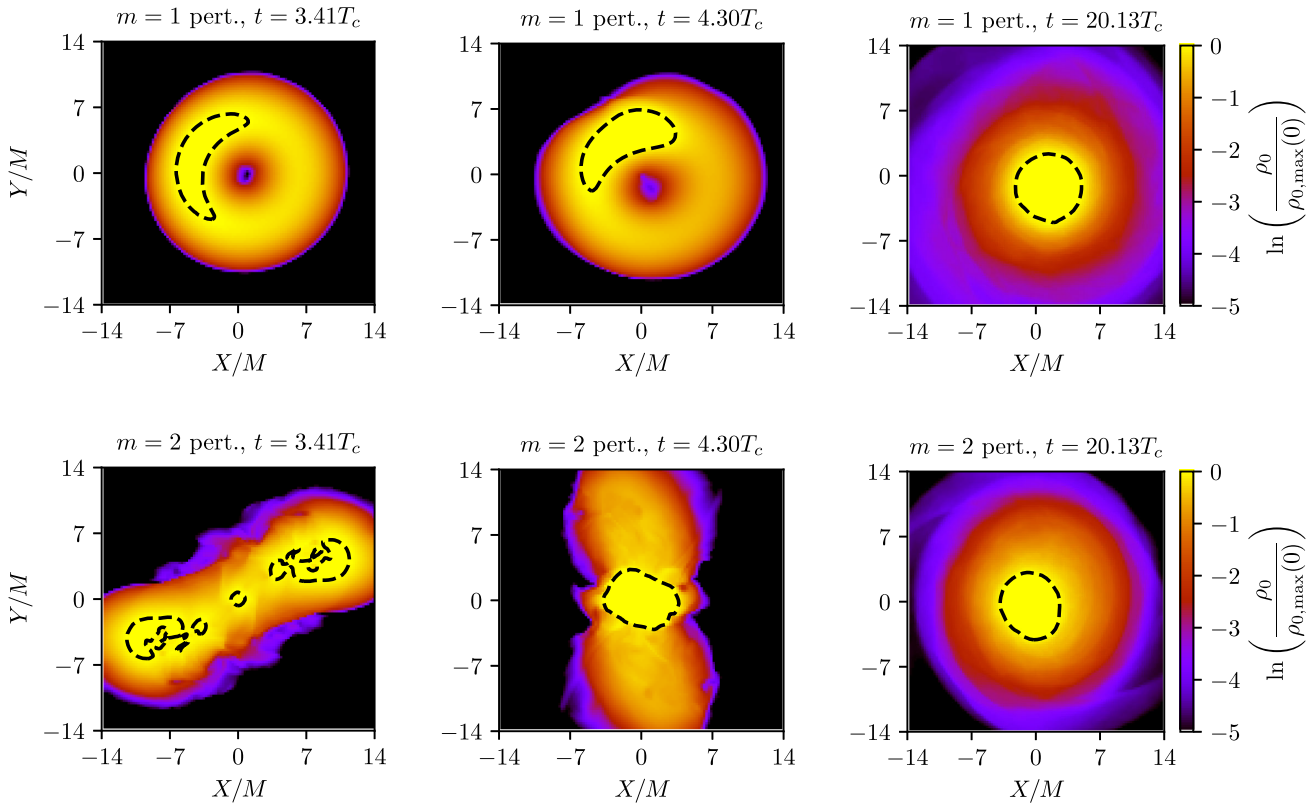

FIG. 9. Snapshots of equatorial contours (i.e., on the X-Y plane) of the rest mass density ρ_0, scaled to the maximum value at the start of simulation $\rho_{0,\max}(0)$ for model $\mathrm{B_{low}}$ under nonaxisymmetric initial perturbations. The top (bottom) panels show the evolution under an initial $m = 1$ ($m = 2$) perturbation. The right panels show the final states in both cases. The dashed curves outline the boundary of the regions within which the rest mass density satisfies $\rho_0 \geq \rho_{0,\max}(0)$.

Model $\mathrm{C_{low}}$ collapses to form a BH earlier in the case of an $m = 1$ initial perturbation than for an $m = 2$ initial perturbation. This suggests that the one-arm mode may be growing on a faster timescale than the bar mode. However, the fact that in the $m = 1$ initial perturbation the collapse does not occur much earlier than in the equilibrium or pressure depletion cases suggests that the mode we excite seeds the unstable mode eigenfunction, but may not be the true eigenfunction. Nevertheless, the general result is consistent with our findings for the high rest mass B

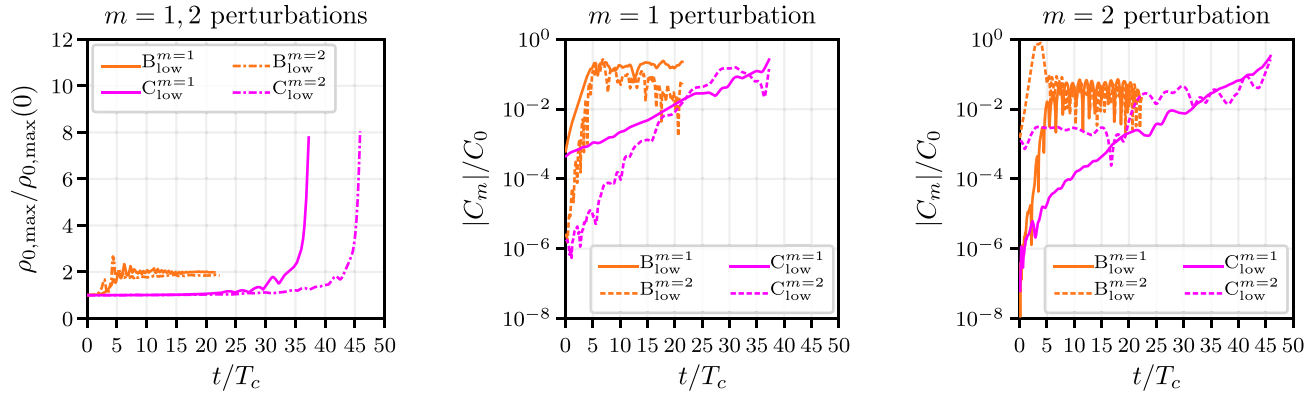

FIG. 10. Left panel: Maximum rest mass density as a function of time for the $\mathrm{B_{low}}$ and $\mathrm{C_{low}}$ models in the case of nonaxisymmetric $m = 1$ (solid lines) and $m = 2$ (dash-dotted lines) rest mass density initial perturbations. The orange and magenta lines correspond to the $\mathrm{B_{low}}$ and $\mathrm{C_{low}}$ models, respectively. Center panel: Evolution of the dominant $m = 1$ (solid lines) and $m = 2$ (dashed lines) nonaxisymmetric density modes for the $\mathrm{B_{low}}$ (orange lines) and $\mathrm{C_{low}}$ models (magenta lines) in the case of an $m = 1$ initial perturbation. Right panel: Same as the center panel but for an $m = 2$ initial perturbation.

and C models (see the left panel of Fig. 6), i.e., the nonaxisymmetric mode that is excited first dominates the subsequent evolution.

Regardless of the details, our results demonstrate the importance of $m = 1$ modes, as has already been pointed out in the studies of NS mergers in [69], where a one-arm instability develops in long-lived remnants. In addition, our calculations demonstrate the significance of an $m = 1$ mode in triggering catastrophic collapse. Therefore, imposing π-symmetry in BNS merger calculations, which is often employed to save computational resources (e.g., [23,78–81]), should be avoided.

C. Gauge-invariant measure of nonaxisymmetric mode development

As discussed in Sec. III C, the density mode decomposition using Eq. (11) is a gauge-dependent diagnostic of the dominant modes that develop during the evolution. To ensure the features of evolution discussed thus far are not gauge artifacts, we also study the gravitational wave signatures using the Newman-Penrose formalism. We focus on two representative cases that include one massive model that collapses to a BH (the C model) and our low-mass model the (B_{low}) that does not undergo collapse. In particular, the evolutions we consider here are the C model under no explicit initial perturbations and B_{low} under an $m = 1$ initial perturbation.

In Fig. 11, we show the real part of the $s = -2$ spin-weighted spherical harmonic modes $\Psi_4^{l,m}$. In general, the same conclusions reached by studying the density modes C_m may be reached if we consider $\Psi_4^{2,m}$ as a measure of nonaxisymmetric mode growth. We find that quasitoroidal stars exhibit growth of the $m = 1$ and $m = 2$ GW modes, even in cases where neither of these modes were explicitly excited. However, the relative amplitude of the GW modes is not the same as in the density mode decomposition. For example, even when an $m = 1$ mode is initially excited, the GW $m = 1$ mode does not dominate over the $m = 2$ mode (as shown in the right panel of Fig. 11). Moreover, in the case of the B_{low} model we find that the $m = 2$ mode remains dominant until the end of the simulation, but with a very small amplitude. Nevertheless, in all cases considered, we observe strong growth of quasiradial and nonaxisymmetric modes consistent with the results presented in Secs. IV A and IV B.

V. DISCUSSION

In this section, we further discuss the results of our simulations and compare them with the results in the literature on differentially rotating $\Gamma = 2$ polytropes. We focus on the role that different properties may play in the evolution of our initial data. We also discuss further the final state that model B_{low} reaches after it settles, and the implications of our findings on cosmic censorship and the fragmentation instability of quasitoroids.

A. Role of $T/|W|$

Generally we find that our massive quasitoroidal models with large values of $T/|W|$ collapse on short timescales due to the growth of nonaxisymmetric modes. It is possible that for a given degree of differential rotation there exists a critical value of $T/|W|$ which signals the onset of instability to nonaxisymmetric modes for quasitoroidal neutron stars described by a $\Gamma = 2$ polytropic EOS. In [74], bounds were placed on the critical value $T/|W|_{crit}$ which indicates dynamical instability to the growth of the bar mode for $\Gamma = 2$ quasitoroids when $\hat{A}^{-1} = 1$ and for masses $1\,M_\odot - 2.5\,M_\odot$ assuming a polytropic constant $\kappa = 165 M_\odot^2$.

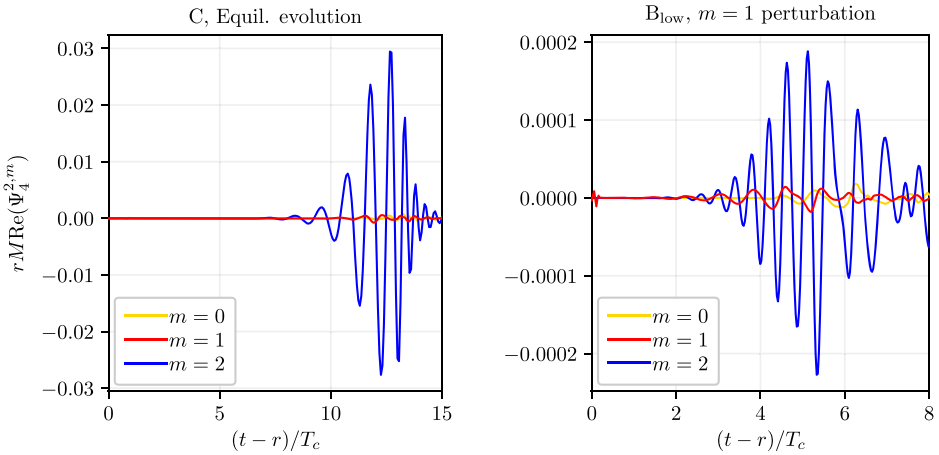

FIG. 11. The real part of the Newman-Penrose scalar $s = -2$ spin-weighted spherical harmonic modes $\Psi_4^{2,m}$ (multiplied by the coordinate radius of the extraction spherical surface r and the ADM mass M) as a function of $t - r$ (scaled by the central period T_c) for two representative evolutions presented in this work. We focus on the contribution from the dominant $l = 2$, $m = 0$ (yellow lines), $m = 1$ (red lines), and $m = 2$ (blue lines) modes. The model and type of perturbation are shown at the top of each panel.

The following fit for $T/|W|_{\rm crit}$ as a function of the rest mass was derived for $\Gamma = 2$ quasitoroidal models,

$$T/|W|_{\rm crit}(M_0) = 0.2636 - 0.0047\frac{M_0}{M_\odot} = 0.2636 - 0.0108\frac{M_0}{M^{\rm TOV}_{0,\rm max}} \quad (12)$$

such that all $\Gamma = 2$ quasitoroids of rest mass M_0 with $T/|W| < T/|W|_{\rm crit}$ should be dynamically stable against the growth of the bar mode instability. We can now test the applicability of Eq. (12) to our models. We convert from polytropic units to units of $M_\odot$ by using the value of the polytropic constant adopted in [74]. The $C_{\rm low}$ model considered in this work is the model with the lowest value of $T/|W|$ which is unstable to the growth of a dynamical bar mode. Inserting the rest mass $M_0^{C_{\rm low}} \simeq 4.18 M_\odot$ of the $C_{\rm low}$ model into Eq. (12), we find a critical value of $T/|W|^{C_{\rm low}}_{\rm crit} = 0.244$, suggesting that all $\Gamma = 2$ quasitoroidal stars of rest mass equal that of the $C_{\rm low}$ model and with $T/|W| < T/|W|^{C_{\rm low}}_{\rm crit}$ should be stable against the growth of a dynamical bar mode. We find that the $C_{\rm low}$ model slightly violates this bound, as it has $T/|W| = 0.238 \approx 0.98\, T/|W|^{C_{\rm low}}_{\rm crit}$ and is still unstable to the growth of a dynamical bar mode. However, the violation is not significant, and we cannot conclude that Eq. (12) is inconsistent with our findings. Further studies are necessary to probe the applicability of Eq. (12). As discussed in Sec. IV, all quasitoroidal models considered in this work were unstable to nonaxisymmetric mode growth. Considering a similar analysis to that provided above for the $C_{\rm low}$ model, we find that all quasitoroidal models respect the bound on $T/|W|_{\rm crit}$ set by Eq. (12). This suggests that the applicability of Eq. (12) may be extended to $\hat{A}^{-1} \neq 1$ and well outside the mass range studied in [74].

However, our quasitoroidal models are unstable not only to the bar mode but also to the one-arm mode. A similar study to that presented in [74] and a derivation of a formula similar to Eq. (12) but with a focus on the growth of the one-arm mode are needed to determine the stability of quasitoroidal $\Gamma = 2$ configurations against the growth of the $m = 1$ mode, but is outside of the scope of this work. We also point out that our model A has $T/|W| \sim 0.3$ and does not develop any nonaxisymmetric modes. Therefore, our study demonstrates that $T/|W|$ alone does not determine the type of instability in a differentially rotating configuration. This is consistent with the existence of the low-$T/|W|$ instability.

B. Role of the rest mass

In our simulations, the value of M_0 appears to control the final state of the configuration, i.e., whether the configuration collapses to a black hole on a dynamical time. Coincidentally, all of our models, except A and $B_{\rm low}$, have rest masses which well exceed the threshold mass for prompt collapse found in BNS merger simulations of $\Gamma = 2$ polytropes [47] ($M_0^{C_{\rm low}} > 1.75 M^{\rm TOV}_{0,\rm max}$), and all of these models undergo collapse to BH on dynamical timescales. By contrast, the $B_{\rm low}$ model does not collapse to a BH by the end of the simulation and shows no signs that collapse will ensue. This model's rest mass $M_0^{B_{\rm low}} = 1.36 M^{\rm TOV}_{0,\rm max}$ is lower than the lower bound on the threshold rest mass $1.65 M^{\rm TOV}_{0,\rm max}$ for prompt collapse to a BH [47].

Although the above discussion suggests that even in isolated rotating neutron star models, the total rest mass controls whether there will be a collapse to a BH on dynamical timescales, we point out that the dimensionless angular momentum of model $B_{\rm low}$ is higher than all other cases and larger than in BNS mergers. This excess angular momentum may provide additional centrifugal support against collapse. More models need to be considered for a complete study, as well as to test whether the threshold mass for prompt collapse found in BNS mergers also provides the line of stability against collapse in isolated neutron stars that may model BNS merger remnants. This is related to the study of [82] who derived the threshold mass for prompt collapse by the use of rotating *spheroidal* neutron star models.

C. Final state of the $B_{\rm low}$ model

Given that model $B_{\rm low}$ does not collapse to a BH, an interesting question is whether this model evolves to the same final, dynamically stable configuration under all evolutions considered. Moreover, given the presence of shocks during the evolutions it is also interesting to test whether significant thermal pressure support exists. In this section we investigate these questions.

Shocks arise during the evolution, and the amount of shock heating differs between the one-arm mode and bar mode evolutions. To test for the impact of shock heating we exploit the fact that the total fluid pressure p can be expressed as a sum of the cold pressure $p_{\rm cold}$ and thermal pressure $p_{\rm therm}$,

$$p = p_{\rm cold} + p_{\rm therm}, \quad (13)$$

where the cold part of the EOS is described by Eq. (4). Our initial models are cold, i.e., $p_{\rm therm} = 0$ at $t = 0$. As the evolution proceeds, shock heating can take place and $p_{\rm therm}$ grows. The separation in Eq. (13) allows us to determine the contribution from the thermal pressure in the final configuration as follows:

$$\frac{p_{\rm therm}}{p_{\rm cold}} = \frac{p}{\kappa \rho_0^2} - 1. \quad (14)$$

If the thermal pressure is a significant component of the total pressure, it may be that the final configuration is

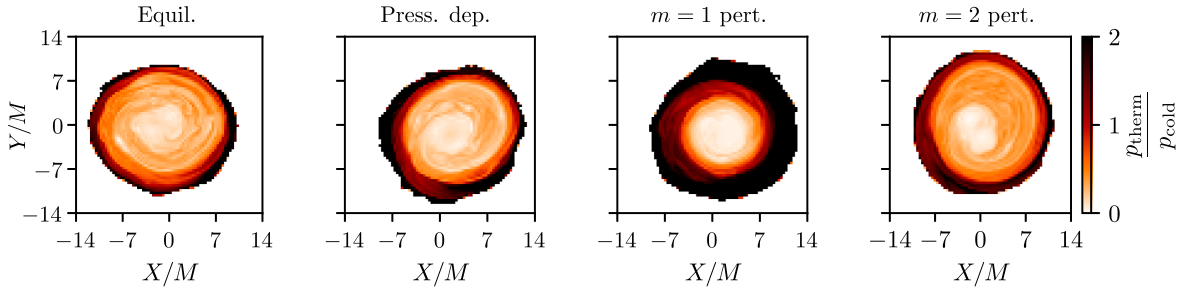

FIG. 12. Contour of the ratio of thermal pressure to cold pressure on the equatorial plane (i.e., on the X-Y plane) corresponding to the final state of the $B_{\rm low}$ model under all initial perturbations. Only densities with $\rho_0 \geq 10^{-3}\rho_{0,\rm max}$ are shown, where $\rho_{0,\rm max}$ corresponds to the maximum rest mass density at the time of the snapshots. All snapshots correspond to $t = 20.13T_c$; the second from the right and rightmost snapshots corresponds to the top and bottom right panels of Fig. 9 for the $m = 1$ and $m = 2$ perturbations, respectively.

possible only because of additional thermal support. This would imply that if the configuration were allowed to cool, it might collapse to a BH [24]. In Fig. 12 we show snapshots of equatorial contours of $p_{\rm therm}/p_{\rm cold}$ after the configurations in the different $B_{\rm low}$ evolutions have settled down to an approximately steady state at $t = 20.13T_c$. We focus on regions where the density is $\rho_0 \geq 10^{-3}\rho_{0,\rm max}$, where the bulk of the matter is. We find similar results under all evolutions, where thermal support near the end of the simulation is small in the regions near the core. The thermal pressure can be significant slightly outside the core and in regions farther out. Therefore, the remnants are primarily cold, but have experienced different amounts of shock heating. Cases with a dominant $m = 2$ mode during the early stages of the evolution (i.e., the equilibrium evolution, pressure depletion, and $m = 2$ initial perturbation) look more similar amongst themselves, and distinct from the case where an $m = 1$ initial perturbation is excited.

Figure 13 shows the time and azimuthally averaged radial rotation profiles, i.e., angular velocity ($\Omega_z = u^\phi/u^t$) in the z direction vs distance on the equatorial plane, that correspond to the final states of model $B_{\rm low}$ shown in Fig. 12. Also shown is the initial angular velocity profile. The plot is only meant to be illustrative, because the angular velocity we compute is not gauge invariant unlike the initial angular velocity. We average the rotational profiles over the azimuthal direction, while accounting for the shift of the configuration's center of rest mass from the initial center of mass, i.e., the coordinate origin. We also average the rotational profiles over a time window of $\Delta t \simeq T_c$. We find that changing the value of the time window for time averaging in the range $0.5T_c \lesssim \Delta t \lesssim 2T_c$ results in a change of the central value of Ω of $\lesssim 10\%$, while the values for $r \gtrsim M$ change by $\lesssim 1\%$.

The rotation profiles of the final state of the $B_{\rm low}$ model are distinct from each other. All final configurations are highly differentially rotating. Steep gradients are seen near the center of the configurations for the equilibrium evolution and $m = 2$ perturbation cases, corresponding to high differential rotation in the innermost region near the core. The central regions in the cases of pressure depletion and for an $m = 1$ perturbation show profiles with relatively lower amounts of differential rotation, and the angular velocity instead increases away from the core. The central region is surrounded by a distribution of matter with decreasing angular velocity for $r \gtrsim 5M$ in all cases. Taking the final angular velocity profiles at face value, it does not appear possible to approximate the angular velocity of these configurations by the one parameter KEH rotation law in Eq. (5), due to their nonmonotonic nature. As such, we do not try to approximate the final states of the $B_{\rm low}$ evolutions with stars described by the KEH law. We conclude that the final states reached in

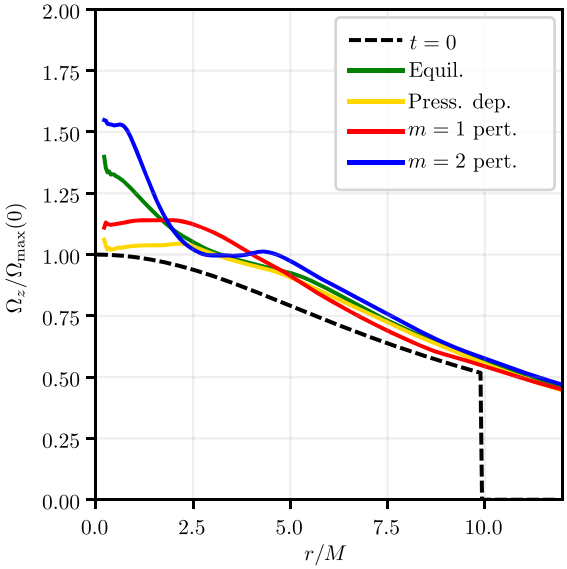

FIG. 13. Azimuthally and time-averaged angular velocity (normalized by the initial maximum angular velocity) vs distance on the equatorial plane in the case of equilibrium evolution (green line), pressure depletion (yellow line), $m = 1$ initial perturbation (red line), and $m = 2$ initial perturbation (blue line) near the end of the simulations. The dashed black line corresponds to the initial angular velocity profile.

different evolutions of the B_{low} model are close to each other but not identical, as was already suggested by the different values of maximum rest mass density to which they settle.

D. Fragmentation instability and cosmic censorship

Our initial data range over values of the dimensionless spin parameter J/M^2 which are both less than and greater than the Kerr bound. If cosmic censorship holds [83], models with $J/M^2 > 1$ will not be able to form a BH unless they shed or redistribute angular momentum through mass ejection, gravitational waves, or other mechanisms [52] or possibly fragment [70].

In all collapsing cases, we were able to locate only a single AH, and the evolution of the lapse function is consistent with a single BH forming. Therefore, we do not find that our stars could collapse to form binary black holes as in [84], even in the most massive cases.

In [52], dynamically unstable, differentially rotating, supra-Kerr models of $\Gamma = 2$ neutron stars could not be found and supra-Kerr models could only be induced to collapse through severe pressure depletion. In this work we found that dynamically unstable supra-Kerr models do exist for $\Gamma = 2$ polytropes (for instance, both the B and C models collapsed to a BH on dynamical timescales even in the case of equilibrium evolution). None of the dynamically unstable supra-Kerr models were found to produce naked singularities. In all cases where the resulting BHs were evolved long enough to settle into approximately steady states, we find that they are surrounded by disks with rest masses as large as 18% the rest mass of the initial configuration. The BHs that form in all cases that undergo catastrophic collapse (initially either sub- or supra-Kerr) have dimensionless spin parameter $a \simeq 0.85$, and hence are not close to unity. We have checked that GWs carry away $O(1\%)$ of the initial angular momentum, and that total angular momentum is conserved to within 1%. The above imply that the remnant disks carry a significant amount of the initial angular momentum. These simulations provide yet another example in which cosmic censorship is respected.

VI. CONCLUSIONS

In this work we performed dynamical simulations in full general relativity to investigate the stability of differentially rotating, high mass spheroidal, and quasitoroidal $\Gamma = 2$ polytropic models of neutron stars. Compared to previous works studying the stability of differentially rotating hypermassive neutron stars, our work probes a part of the parameter space that has not been probed before, namely the part corresponding to highly quasitoroidal, and very massive stars (as massive as ~4 times the TOV limit mass). Recent work, which discovered these extreme configurations, suggested that massive quasitoroidal configurations could have important consequences for neutron star mergers or core collapse supernovae. Indeed, the existence of such massive equilibria might suggest that much more massive remnants than previously found could exist in these astrophysical scenarios. But, for this to be the case, such extreme quasitoroidal configurations would have to be dynamically stable. Thus, here we initiated a study of the dynamical stability of these extreme equilibria.

Four of the five initial equilibria we investigated are quasitoroidal: models B and C, which are the most massive, and models B_{low} and C_{low}, with masses closer to remnants that could form following a BNS merger. The fifth initial configuration we considered is the most massive (type A) spheroidal star, also with an astrophysically relevant rest mass. Apart from model B_{low}, we found that all models underwent catastrophic collapse to single BHs under various types of initial perturbations or no perturbations at all. The most massive spheroidal model was unstable only against a quasiradial perturbation. By contrast, all quasitoroidal configurations were unstable to the development of nonaxisymmetric instabilities. We found that the dominant nonaxisymmetric modes are either the $m = 1$ or the $m = 2$ modes, which grow on very similar timescales. Our simulations indicate that the first nonaxisymmetric mode to be seeded early on in the evolution of a quasitoroidal star is the mode that dominates the evolution. Thus, when the $m = 1$ mode is excited, a one-arm instability takes over; whereas when the $m = 2$ mode is excited, a bar mode instability dominates. We find that in some cases the one-arm mode may dominate over the bar mode, when no explicit perturbations are seeded initially, but perturbations are always excited at the level of truncation error in our simulations because our grid coordinates are slightly shifted to avoid the origin. Our findings further demonstrate the importance of the $m = 1$ mode for the stability of differentially rotating neutron stars that was recently pointed out in [22,69,73].

We considered the role that the ratio of rotational kinetic energy to gravitational binding energy $T/|W|$ played in the stability of these equilibria. We find that the prediction of [74] (which applies to a particular degree of differential rotation and a certain range of masses) for the critical value $T/|W|_{crit}$ marking the onset of the dynamical bar mode instability is largely consistent with the models studied here. Our model C_{low}, with the lowest value of $T/|W|$, slightly violates the prediction but we cannot conclude that it is inconsistent with it. However, we study models with $T/|W| > T/|W|_{crit}$ that do not undergo the bar mode instability, indicating that there are other important parameters at play for a configuration to be unstable to the bar mode instability. We also considered the role of the rest mass in determining the final state of quasitoroidal configurations. Our study suggests that the total rest mass appears to determine primarily whether collapse to BH will

ensue. However, more detailed studies are necessary to solidify these conclusions.

Our lowest-mass quasitoroidal model (B_{low}) underwent a transition to a spheroidal solution either through a bar mode or a one-arm mode instability, depending on the mode that is excited first. However, we did not excite higher nonaxisymmetric modes, and it is conceivable that all quasitoroidal models we considered are unstable against $m > 2$ modes, too [85]. We find that the dynamically found, highly differentially rotating, quasistationary, spheroidal solutions resulting from the evolution of model B_{low} are similar to but distinct from each other. These final configurations have a small thermal pressure component at their cores, but thermal pressure is non-negligible far from the core. We also found that their angular velocity profiles do not appear to be reasonably approximated by the KEH rotation law. All of the final states of the B_{low} model are dynamically stable, but secularly unstable due to dissipative effects.

We investigated the properties of the BHs formed in the collapsing models, and we found that all resulting BHs have high dimensionless spin (about 0.85) by the end of simulation and cosmic censorship is always respected even when the initial solutions exceed the Kerr limit. We did not find evidence of the formation of multiple BHs. Our study explicitly shows that exceeding the Kerr bound initially does not imply the dynamical stability of a rotating stellar configuration.

Our work shows that the existence of extreme quasitoroidal neutron star equilibrium solutions, which support a mass well exceeding the BNS threshold mass for prompt collapse to a BH, does not imply that BNS merger remnants can be very massive, too. Moreover, highly quasitoroidal models of neutron stars appear to be dynamically unstable against the development of nonaxisymmetric instabilities, and will either collapse to a BH or transition to a dynamically stable, spheroidal, differentially rotating configuration.

A few caveats for the present work are in order. First, we did not scan the entire solution space of differentially rotating quasitoroidal solutions, nor did we build our initial models to correspond to a particular sequence (i.e., constant rest mass or constant angular momentum sequences). The rationale in this work was to probe the most massive, differentially rotating configurations recently found in the literature and to include a few lower mass models of the quasitoroidal type to test if configurations more massive than what is achievable in BNS mergers can be dynamically stable. More realistic descriptions of the matter may play an important role in the evolution of quasitoroidal models, but we do not expect it to change our basic conclusion that massive, quasitoroidal models of neutron stars built with the KEH differential rotation law are generically dynamically unstable. In particular, analogous models to those studied here described by the KEH rotation law have been shown to exist for realistic, hybrid hadron-quark, and strange quark matter equations of state [18,19,21]. The KEH law may not suitably describe the remnants of BNS mergers [69,86,87]. More realistic rotation laws [88] could possibly lead to different stability properties of quasitoroidal stars. Finally, the effects of magnetic fields could significantly affect the evolution of quasitoroids. Magnetic braking and turbulent magnetic viscosity may act to remove differential rotation on short timescales [75–77,89], leading to faster collapse in the types of stars studied here. We leave a more systematic investigation of all these topics for future work.

ACKNOWLEDGMENTS

P. E. and V. P. thank KITP for hospitality during the GRAVAST19 program, where part of this work was completed. This research was supported in part by National Science Foundation (NSF) Grant No. PHY-1912619 at the University of Arizona, NSF Grant No. PHY-1662211, and NASA Grant No. 80NSSC17K0070 at the University of Illinois at Urbana-Champaign, NSF Grant No. PHY-1707526 to Bowdoin College, and through sabbatical support from the Simons Foundation (Grant No. 561147 to T. W. B.). The simulations presented in this work were carried out in part on the Ocelote and ElGato clusters at the University of Arizona, the Blue Waters supercomputer at NCSA, and the Stampede2 cluster at TACC under XSEDE allocation PHY180044. Research at KITP. is supported in part by the National Science Foundation under Grant No. NSF PHY-1748958. The Blue Waters sustained-petascale computing project is supported by the National Science Foundation (Grants No. OCI-0725070 and No. ACI-1238993) and the State of Illinois. Blue Waters is a joint effort of the University of Illinois at Urbana-Champaign and its National Center for Supercomputing Applications.

APPENDIX: RESOLUTION STUDY AND GRID EFFECTS

In this Appendix we discuss the results of our resolution study for a subset of the models presented in Table I. We also discuss the effects of shifting the computational grid to avoid the origin of the coordinate system.

For model A in the case of pressure depletion and model B under both $m = 1$ and $m = 2$ perturbations we performed runs at 1.2 and 1.5 times the resolution of the canonical resolution discussed in Sec. III A. We find that our results are qualitatively invariant with resolution, and that they exhibit approximate second order convergence, which is the order of accuracy of our hydrodynamic numerical scheme. More specifically, the dominant unstable modes are invariant with resolution, and all collapsing models collapse to BHs with properties that are consistent with the canonical simulations discussed in Sec. V.

We demonstrate convergence using the evolution of model B under an $m = 2$ perturbation. In the left panel of Fig. 14 we show the difference of $|\Psi_4^{2,2}|$ between the

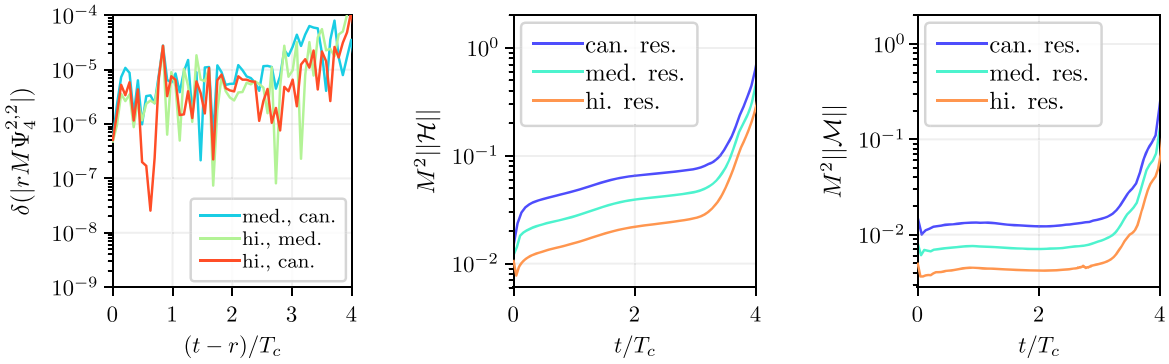

FIG. 14. Left panel: Convergence of $|\Psi_4^{2,2}|$ as a function of $(t-r)/T_c$ in the case of the B model under an $m=2$ perturbation. The left panel shows the difference of $|\Psi_4^{2,2}|$ between the medium and canonical resolution runs (cyan line, labeled "med., can."), the medium and high resolution runs (green line, labeled "hi., med."), and the high and canonical resolution runs (orange line, labeled "hi., can."), scaled assuming second order convergence. Center panel: L2 norm of the Hamiltonian constraint times the squared ADM mass $M^2||\mathcal{H}||$ as a function of time for the B model under an $m=2$ perturbation. Shown are the canonical (blue line), medium (cyan line), and high (orange line) resolution runs. Right panel: Same as the center panel, but for the L2 norm of the momentum constraint $||\mathcal{M}||$.

medium and canonical resolutions, between the high and medium resolutions, and between the high and canonical resolutions. The curves have been scaled assuming second order convergence, and the overlap between them indicates approximate second order convergence.

In the center and right panels of Fig. 14, we show the L2 norm of the Hamiltonian and momentum constraints, respectively, times the squared ADM mass M^2 for the canonical, medium, and high resolutions. As is clear the Hamiltonian and momentum constraints are converging to 0 with increased resolution, and the trend is consistent with approximate second order convergence.

In order to avoid coordinate singularities associated with transforming the initial data from spherical polar coordinates to Cartesian, we shift our y coordinates by a small amount to avoid the origin of the coordinate system. To test whether our results are affected by this choice of coordinate grids, we considered a sequence of simulations with decreasing coordinate shift $\delta y \in [0.01, 0.005, 0.001, 0.0001]$. We label each of these shifts as $\delta y_{\rm high}=0.01$, $\delta y_{\rm med}=0.005$, $\delta y_{\rm stand}=0.001$, and $\delta y_{\rm low}=0.0001$ (note that our standard runs employ a grid shift of $\delta y_{\rm stand}$). In Fig. 15 we show the evolution of the dominant nonaxisymmetric modes for this sequence of simulations. It is clear that the results are practically the same for all coordinate shifts.

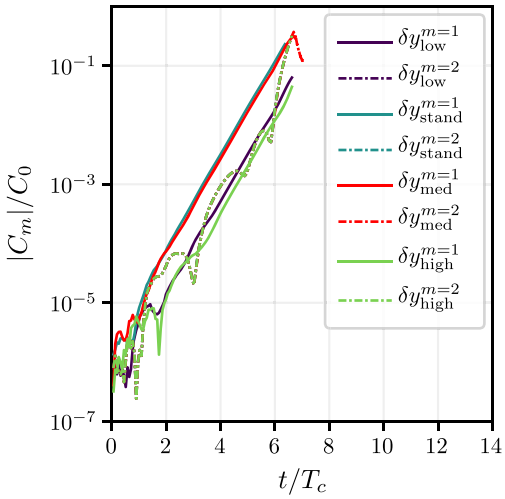

FIG. 15. Density mode decomposition for the shifted grid simulations in the case of the B model under pressure depletion. We show the two most dominant modes, which are always the $m=1$ (solid lines) or $m=2$ (dash-dotted lines) modes. The dark purple lines show the results for a small grid shift $\delta y_{\rm low}=0.0001$, the blue lines show the results for our standard simulations with grid shift $\delta y_{\rm stand}=0.001$, the red lines show the results for a medium sized grid shift $\delta y_{\rm med}=0.005$, and the green lines show the results for a large grid shift $\delta y_{\rm high}=0.01$.

[1] B. P. Abbott *et al.*, Astrophys. J. Lett. **848**, L12 (2017).
[2] M. Shibata, S. Fujibayashi, K. Hotokezaka, K. Kiuchi, K. Kyutoku, Y. Sekiguchi, and M. Tanaka, Phys. Rev. D **96**, 123012 (2017).
[3] M. Ruiz, S. L. Shapiro, and A. Tsokaros, Phys. Rev. D **97**, 021501 (2018).
[4] B. Margalit and B. D. Metzger, Astrophys. J. Lett. **850**, L19 (2017).
[5] A. Bauswein, O. Just, H.-T. Janka, and N. Stergioulas, Astrophys. J. **850**, L34 (2017).
[6] D. Radice, A. Perego, S. Bernuzzi, and B. Zhang, Mon. Not. R. Astron. Soc. **481**, 3670 (2018).

[7] L. Rezzolla, E. R. Most, and L. R. Weih, Astrophys. J. **852**, L25 (2018).
[8] V. Paschalidis, Classical Quantum Gravity **34**, 084002 (2017).
[9] R. Gill, A. Nathanail, and L. Rezzolla, Astrophys. J. **876**, 139 (2019).
[10] L. Baiotti and L. Rezzolla, Rep. Prog. Phys. **80**, 096901 (2017).
[11] B. P. Abbott *et al.* (Virgo and LIGO Scientific Collaborations), Phys. Rev. Lett. **119**, 161101 (2017).
[12] T. W. Baumgarte, S. L. Shapiro, and M. Shibata, Astrophys. J. Lett. **528**, L29 (2000).
[13] G. Cook, S. Shapiro, and S. Teukolsky, Astrophys. J. **398**, 203 (1992).
[14] M. Ansorg, D. Gondek-Rosinska, and L. Villain, Mon. Not. R. Astron. Soc. **396**, 2359 (2009).
[15] D. Gondek-Rosinska, I. Kowalska, L. Villain, M. Ansorg, and M. Kucaba, Astrophys. J. **837**, 58 (2017).
[16] A. M. Studzinska, M. Kucaba, D. Gondek-Rosinska, L. Villain, and M. Ansorg, Mon. Not. R. Astron. Soc. **463**, 2667 (2016).
[17] V. Paschalidis and N. Stergioulas, Living Rev. Relativity **20**, 7 (2017).
[18] P. Espino and V. Paschalidis, Phys. Rev. D **99**, 083017 (2019).
[19] M. Szkudlarek, D. Gondek-Rosińska, L. Villain, and M. Ansorg, Astrophys. J. **879**, 44 (2019).
[20] E. Zhou, A. Tsokaros, K. Uryu, R. Xu, and M. Shibata, arXiv:1902.09361.
[21] G. Bozzola, P. L. Espino, C. D. Lewin, and V. Paschalidis, arXiv:1905.00028.
[22] W. E. East, V. Paschalidis, F. Pretorius, and S. L. Shapiro, Phys. Rev. D **93**, 024011 (2016).
[23] X. Zhang, Z. Cao, and H. Gao, Int. J. Mod. Phys. D **28**, 1950026 (2019).
[24] V. Paschalidis, Z. B. Etienne, and S. L. Shapiro, Phys. Rev. D **86**, 064032 (2012).
[25] N. Stergioulas, A. Bauswein, K. Zagkouris, and H.-T. Janka, Mon. Not. R. Astron. Soc. **418**, 427 (2011).
[26] J. M. Centrella, K. C. B. New, L. L. Lowe, and J. D. Brown, Astrophys. J. Lett. **550**, L193 (2001).
[27] M. Saijo, T. W. Baumgarte, and S. L. Shapiro, Astrophys. J. **595**, 352 (2003).
[28] A. L. Watts, N. Andersson, and D. I. Jones, Astrophys. J. Lett. **618**, L37 (2005).
[29] S. Ou and J. E. Tohline, Astrophys. J. **651**, 1068 (2006).
[30] M. Saijo and S. Yoshida, Mon. Not. R. Astron. Soc. **368**, 1429 (2006).
[31] D. Radice, S. Bernuzzi, and C. D. Ott, Phys. Rev. D **94**, 064011 (2016).
[32] L. Lehner, S. L. Liebling, C. Palenzuela, and P. M. Motl, Phys. Rev. D **94**, 043003 (2016).
[33] G. Corvino, L. Rezzolla, S. Bernuzzi, R. De Pietri, and B. Giacomazzo, Classical Quantum Gravity **27**, 114104 (2010).
[34] M. Shibata, T. W. Baumgarte, and S. L. Shapiro, Astrophys. J. **542**, 453 (2000).
[35] M. Shibata, S. Karino, and Y. Eriguchi, Mon. Not. R. Astron. Soc. **334**, L27 (2002).
[36] M. Shibata, S. Karino, and Y. Eriguchi, Mon. Not. R. Astron. Soc. **343**, 619 (2003).
[37] P. Cerda-Duran, V. Quilis, and J. A. Font, Comput. Phys. Commun. **177**, 288 (2007).
[38] A. Passamonti and N. Andersson, Mon. Not. R. Astron. Soc. **446**, 555 (2015).
[39] M. Saijo and S. Yoshida, Phys. Rev. D **94**, 084032 (2016).
[40] S. Yoshida and M. Saijo, Mon. Not. R. Astron. Soc. **466**, 600 (2017).
[41] G. Bozzola, N. Stergioulas, and A. Bauswein, Mon. Not. R. Astron. Soc. **474**, 3557 (2018).
[42] L. R. Weih, E. R. Most, and L. Rezzolla, Mon. Not. R. Astron. Soc. **473**, L126 (2018).
[43] J. L. Friedman, Commun. Math. Phys. **63**, 243 (1978).
[44] N. Comins and B. F. Schutz, Proc. R. Soc. A **364**, 211 (1978).
[45] S. Yoshida and Y. Eriguchi, Mon. Not. R. Astron. Soc. **282**, 580 (1996).
[46] V. Cardoso, P. Pani, M. Cadoni, and M. Cavaglia, Phys. Rev. D **77**, 124044 (2008).
[47] M. Shibata, K. Taniguchi, and K. Uryu, Phys. Rev. D **68**, 084020 (2003).
[48] M. Shibata and K. Taniguchi, Phys. Rev. D **73**, 064027 (2006).
[49] A. Bauswein, T. W. Baumgarte, and H. T. Janka, Phys. Rev. Lett. **111**, 131101 (2013).
[50] A. Bauswein, N. Stergioulas, and H. T. Janka, Phys. Rev. D **90**, 023002 (2014).
[51] S. Koeppel, L. Bovard, and L. Rezzolla, Astrophys. J. **872**, L16 (2019).
[52] B. Giacomazzo, L. Rezzolla, and N. Stergioulas, Phys. Rev. D **84**, 024022 (2011).
[53] G. Cook, S. Shapiro, and S. Teukolsky, Astrophys. J. **422**, 227 (1994).
[54] H. Komatsu, Y. Eriguchi, and I. Hachisu, Mon. Not. R. Astron. Soc. **237**, 355 (1989).
[55] G. Cook, S. Shapiro, and S. Teukolsky, Astrophys. J. **424**, 823 (1994).
[56] M. D. Duez, Y. T. Liu, S. L. Shapiro, and B. C. Stephens, Phys. Rev. D **72**, 024029 (2005).
[57] Z. B. Etienne, V. Paschalidis, R. Haas, P. Moesta, and S. L. Shapiro, Classical Quantum Gravity **32**, 175009 (2015).
[58] G. Allen, D. Angulo, I. T. Foster, G. Lanfermann, C. Liu, T. Radke, E. Seidel, and J. Shalf, Int. J. High Perform. Comput. Appl. **15**, 345(2001).
[59] E. Schnetter, S. H. Hawley, and I. Hawke, Classical Quantum Gravity **21**, 1465 (2004).
[60] E. Schnetter, P. Diener, E. N. Dorband, and M. Tiglio, Classical Quantum Gravity **23**, S553 (2006).
[61] M. Shibata and T. Nakamura, Phys. Rev. D **52**, 5428 (1995).
[62] T. W. Baumgarte and S. L. Shapiro, Phys. Rev. D **59**, 024007 (1998).
[63] C. Bona, J. Masso, E. Seidel, and J. Stela, Phys. Rev. Lett. **75**, 600 (1995).
[64] M. Alcubierre, B. Bruegmann, D. Pollney, E. Seidel, and R. Takahashi, Phys. Rev. D **64**, 061501 (2001).
[65] M. Alcubierre, B. Bruegmann, P. Diener, M. Koppitz, D. Pollney, E. Seidel, and R. Takahashi, Phys. Rev. D **67**, 084023 (2003).

[66] Z. B. Etienne, J. A. Faber, Y. T. Liu, S. L. Shapiro, K. Taniguchi, and T. W. Baumgarte, Phys. Rev. D **77**, 084002 (2008).
[67] Z. B. Etienne, V. Paschalidis, Y. T. Liu, and S. L. Shapiro, Phys. Rev. D **85**, 024013 (2012).
[68] Z. B. Etienne, Y. T. Liu, and S. L. Shapiro, Phys. Rev. D **82**, 084031 (2010).
[69] V. Paschalidis, W. E. East, F. Pretorius, and S. L. Shapiro, Phys. Rev. D **92**, 121502 (2015).
[70] B. Zink, N. Stergioulas, I. Hawke, C. D. Ott, E. Schnetter, and E. Mueller, Phys. Rev. D **76**, 024019 (2007).
[71] J. Thornburg, Classical Quantum Gravity **21**, 743 (2004).
[72] M. Alcubierre, B. Brügmann, P. Diener, F. S. Guzmán, I. Hawke, S. Hawley, F. Herrmann, M. Koppitz, D. Pollney, E. Seidel, and J. Thornburg, Phys. Rev. D **72**, 044004 (2005).
[73] W. E. East, V. Paschalidis, and F. Pretorius, Classical Quantum Gravity **33**, 244004 (2016).
[74] F. Löffler, R. De Pietri, A. Feo, F. Maione, and L. Franci, Phys. Rev. D **91**, 064057 (2015).
[75] S. L. Shapiro, Astrophys. J. **544**, 397 (2000).
[76] M. D. Duez, Y. T. Liu, S. L. Shapiro, and B. C. Stephens, Phys. Rev. D **69**, 104030 (2004).
[77] M. D. Duez, Y. T. Liu, S. L. Shapiro, M. Shibata, and B. C. Stephens, Phys. Rev. Lett. **96**, 031101 (2006).
[78] L. Baiotti, R. De Pietri, G. M. Manca, and L. Rezzolla, Phys. Rev. D **75**, 044023 (2007).
[79] G. M. Manca, L. Baiotti, R. De Pietri, and L. Rezzolla, Classical Quantum Gravity **24**, S171 (2007).
[80] L. Rezzolla, L. Baiotti, B. Giacomazzo, D. Link, and J. A. Font, Classical Quantum Gravity **27**, 114105 (2010).
[81] B. Giacomazzo, L. Rezzolla, and L. Baiotti, Phys. Rev. D **83**, 044014 (2011).
[82] A. Bauswein and N. Stergioulas, Mon. Not. R. Astron. Soc. **471**, 4956 (2017).
[83] R. Penrose, Riv. Nuovo Cimento **1**, 252 (1969); Gen. Relativ. Gravit. **34**, 1141 (2002).
[84] C. Reisswig, C. D. Ott, E. Abdikamalov, R. Haas, P. Moesta, and E. Schnetter, Phys. Rev. Lett. **111**, 151101 (2013).
[85] J. L. Friedman and B. F. Schutz, Astrophys. J. **222**, 281 (1978).
[86] E. B. Abdikamalov, H. Dimmelmeier, L. Rezzolla, and J. C. Miller, Mon. Not. R. Astron. Soc. **392**, 52 (2009).
[87] F. Galeazzi, S. Yoshida, and Y. Eriguchi, Astron. Astrophys. **541**, A156 (2012).
[88] K. Uryu, A. Tsokaros, L. Baiotti, F. Galeazzi, K. Taniguchi, and S. Yoshida, Phys. Rev. D **96**, 103011 (2017).
[89] M. Ruiz, A. Tsokaros, V. Paschalidis, and S. L. Shapiro, Phys. Rev. D **99**, 084032 (2019).